Science and Technology of Advanced Materials

ISSN: 1468-6996 (Print) 1878-5514 (Online) Journal homepage: www.tandfonline.com/journals/tsta20

Room-temperature bulk photovoltaic effect in a terthiophene-based ferroelectric liquid crystal bearing dilactate side chains

Masahiro Funahashi, Yasuko Koshiba, Shohei Horike & Shinobu Uemura

To cite this article: Masahiro Funahashi, Yasuko Koshiba, Shohei Horike & Shinobu Uemura (01 Jul 2025): Room-temperature bulk photovoltaic effect in a terthiophene-based ferroelectric liquid crystal bearing dilactate side chains, Science and Technology of Advanced Materials, DOI: 10.1080/14686996.2025.2525058

To link to this article: https://doi.org/10.1080/14686996.2025.2525058

Publisher: Taylor & Francis & The Author(s). Published by National Institute for Materials Science inpartnership with Taylor & Francis Group.
Journal: *Science and Technology of Advanced Materials*
DOI: 10.1080/14686996.2025.2525058

Room-temperature bulk photovoltaic effect in a terthiophene-based ferroelectric liquid crystal bearing dilactate side chains

Masahiro Funahashi*[a,b,e], Yasuko Koshiba[a,b], Shohei Horike[a,b,c], and Shinobu Uemura[d,e]

[a] *Department of Chemical Science and Engineering, Graduate School of Engineering, Kobe University.*

[b] *Research Center for Membrane and Film Technology, Kobe University.*

[c] *Center for Environmental Management, Kobe University, 1-1 Rokkodai, Nada-ku, Kobe, Hyogo 657-8501, Japan.*

[d] *Program in Advanced Materials Science, Faculty of Engineering and Design, Kagawa University, 2217-20 Hayashi-cho, Takamatsu, Kagawa 761-0396, Japan*

[e] *Health and Medical Research Institute, National Institute of Advanced Industrial Science and Technology, 2217-14 Hayashi-cho, Takamatsu, Kagawa 761-0395, Japan*

funahashi.masahiro@phoenix.kobe-u.ac.jp

Room-temperature bulk photovoltaic effect in a terthiophene-based ferroelectric liquid crystal bearing dilactate side chains

Room-temperature bulk photovoltaic effect of a ferroelectric liquid crystal based on diphenylterthiophene bearing dilactate side chains is provided in this study. In the polarized smectic phase of this compound, the improved bulk photovoltaic effect was observed without electron acceptors, indicating the open-circuit voltage of 1.1 V. A time-of-flight measurement revealed that the hole and electron mobilities were retained to be over 1×10^{-3} $cm^2V^{-1}s^{-1}$ at room temperature. Dielectric relaxation spectra exhibited that the relaxation of dipolar fluctuation shifted from 10^5 Hz to 10^4 Hz in the polarized smectic phase, indicating suppression of thermal motion of the polar side chains. By doping a fullerene derivative as an electron acceptor, the performance of the bulk photovoltaic effect was also enhanced at room temperature, indicating the power conversion efficiency of 0.24 %. The double chiral structure of the dilactate side chain should restrict the conformation of the carbonyl groups in the side chains to enhance packing of the π-conjugated units and to stabilize the polarized structure of the smectic phase.

Keywords: bulk photovoltaic effect; ferroelectric; liquid crystalline semiconductor; oligothiophene; lactate; ferroelectric liquid crystal

1. Introduction

Different from conventional photovoltaic effects based on p-n and Schottky junctions, a bulk photovoltaic effect is driven by a polarization field generated over the bulk of the ferroelectrics [1]. Therefore, an open-circuit voltage of the bulk photovoltaic effect can exceed the bandgaps of the ferroelectrics. Considering a potential to overcome the Shockley-Queisser limit [2], this effect has been studied in inorganic ferroelectrics such as barium titanate, lithium niobate, bismuth ferrite, SbSI, and SnS, as well as chiral ammonium triiodide crystals [3-9]. However, inorganic ferroelectrics have large bandgaps, indicating small photocurrents and low power conversion efficiencies.

Conventional organic ferroelectrics including polymers, charge transfer complexes, and hydrogen-bonding crystals are electrical insulators [10-12]. In order to construct organic bulk photovoltaic systems, extended π-conjugated units should be incorporated in polarized matrices. In poly(vinylidene fluoride) doped with a π-conjugated dye and crystalline films of triphenylene derivatives bearing six ester moieties, high photovoltages were reported although small photocurrent resulted in low power conversion efficiency [13,14]. Shift current originated from a quantum mechanical effect in non-centrosymmetric crystal structures has been reported in charge transfer complexes based on tetrathiafulvalene and chloranil [15]. However, the temperature range of the ferroelectric phase is lower than 90 K and the photovoltaic effect diminishes at room temperature.

Typical ferroelectric liquid crystal (FLC) phase is a chiral smectic C (SmC*) phase in which liquid crystalline (LC) molecules bearing a chiral alkyl chain were self-organized in layers and the molecular axes tilted from the layer normal [16]. As well as the SmC* phase, bent-core liquid crystals, ferroelectric columnar phases, and ferroelectric nematic phase have been studied extensively [17-21]. Efficient electronic charge carrier transports have been observed in columnar, smectic, nematic phases of LC molecules comprising extended π-conjugated units [22-34]. FLCs consisting of extended π-conjugated units and polar side chains exhibit switching behaviors in electronic conduction processes [35-38]. However, a bulk photovoltaic effect has not been reported in these FLCs.

We first reported a bulk photovoltaic effect in the FLCs consisting of extended π-conjugated units and chiral alkyl chains [39,40]. The spontaneous polarization in the SmC* phase can be immobilized in the ordered chiral smectic phases, resulting in an

enhanced bulk photovoltaic effect [41-43]. The bulk photovoltaic effect was also observed in ferroelectric columnar phases of achiral subphthalocyanine derivatives [44-46]. The subphthalocyanine derivatives absorb visible light and indicate the photovoltaic effect for visible light illumination although the open-circuit voltage and power conversion efficiency have been still low.

Enhanced bulk photovoltaic effect has been reported in π-conjugated FLCs bearing lactate ester side chains [47]. Composites of the FLCs and fullerene derivatives exhibited a high open-circuit voltage up to 1.2 V and a high external quantum efficiency for blue and near UV light illumination at room temperature [48,49]. The spectral sensitivity of the photovoltaic effect can be extended to a green light region in FLCs consisting of a quinquethiophene unit and lactate moieties [50]. However, the effective photovoltaic effect was observed only at elevated temperature. In most cases of the bulk photovoltaic effect of FLCs, the performance remarkably lowered at room temperature. The carrier transport in columnar and smectic phases is described by a thermally activated hopping mechanism, resulting in deterioration of carrier mobility below room temperature [51,52]. Polarization relaxation at room temperature also degrades the photovoltaic effect.

In this study, we report a diphenylterthiophene derivative bearing dilactate side chains. This compound exhibits stable photovoltaic characteristics at room temperature. A dilactate moiety is a unit structure of a polylactide which exhibits piezoelectricity and can be a chiral polar moiety of ferroelectric liquid crystals [53]. The current-voltage curves exhibited an ideal diode character under dark and illuminated states, resulting in an improved fill factor. The effective photovoltaic effect was observed even at room temperature. Moreover, polarization relaxation in the bulk was remarkably suppressed,

due to the reduction of thermal motion of the side chains.

2. Experimental

2.1. Materials

Polylactide is a typical piezoelectric polymer. We paid attention to a dilactate structure as a partial unit of polylactide. We synthesized fluorinated diphenylterthiophene derivative (*S*,*S*)-**1** bearing (*S*,*S*)-butyl dilactate side chains, as shown in Scheme 1. Ethyl lactate derivative (*S*)-**2** was hydrolyzed to produce lactic acid derivative (*S*)-**3**, which was condensed with (*S*)-butyl lactate to form dilactate (*S*,*S*)-**4**. By the Pd-catalyzed coupling reaction, dilactate (*S*,*S*)-**4** was converted to borate (*S*,*S*)-**5** [54], which was coupled with 5,5”-dibromo-2,2’:5’,2”-terthiophene by the Suzuki-Miyaura coupling reaction [55] to produce LC compound (*S*,*S*)-**1**. Detailed procedures of the synthesis are indicated in supporting information. Compared to compound **6** reported previously (Scheme 2) [47,48], enhanced polarizability and suppressed mobility of the dilactate side chains should be expected in compound (*S*,*S*)-**1**.

2.2. Characterization of the mesophases

The mesomorphic properties of compounds (*S*,*S*)-**1** was conducted by observation under a polarizing optical microscope, differential scanning calorimetry (DSC), and X-ray diffraction. Optical textures of chiral smectic phases were studied using a polarizing light microscope (POM, Olympus DP70) equipped with a hand-made hot stage. X-ray diffraction patterns of the LC phases were collected by Rigaku Rapid II, Cu Kα1. The phase transition temperatures and the transition enthalpies were determined using NETZSCH Maia DSC 200 F3.

2.3. Polarization of compound (S,S)-1

Because the viscosity of the mesophase of compound (*S*,*S*)-**1** was too high and the speed of the polarization inversion was too slow under a DC electric field over 10^5 V·cm^{-1}. In fact, polarizing optical micrographic texture of the M* phase did not change under a DC field application of 10^5 V · cm^{-1} although it was partially changed by the DC field application for several hours within 1 degree below the phase transition from the isotropic phase. Consequently, the spontaneous polarization of the mesophase could not be determined by the conventional Sawyer-Tower method or polarization inversion current measurement. Alternately, thermally stimulated current [56] was measured on heating at a rate of 0.25 K·min^{-1} from the mesophase to the isotropic phase. Polarization was estimated from the integration of the thermally stimulated current across the phase transition. Besides, the change of the optical texture of the mesophase of compound (*S*,*S*)-**1** was observed by a POM under an application of a DC bias.

2.4. Photovoltaic effect measurement in sandwich cells

The 2 μm- and 4 μm-thick LC cells consisting of ITO-coated glass substrates (EHC, Japan) were used for the measurements of the bulk photovoltaic effect. A cell capillary-filled with compound (*S*,*S*)-**1** or the compound doped with [6,6]-Phenyl-C61-Butyric Acid Methyl Ester (PCBM, 8 wt %) was heated to 120 ˚C on a hot stage and cooled to the phase transition temperature to the mesophase. A DC bias (20 V or 10 V for a 4 μm- or 2 μm-thick sample, respectively) for a poling treatment was applied to the cell and cooled to 30 °C in 30 min. White light (3.5 W LED, 20 mWcm^{-2}) was illuminated on the cell at 30 °C and photocurrent was measured varying the applied voltage, using an electrometer Keithley 6517A.

2.5. Characterization of carrier transport

The carrier mobilities were determined by a time-of-flight (TOF) method under atmospheric conditions [57]. The LC sample in the isotropic phase was capillary-filled into a cell consisting of two ITO-coated glass plates on a hot stage. The third harmonic generation of a Nd:YAG pulse laser (Continuum MiniLite II, wavelength = 356 nm) was used for excitation of the samples. The laser pulses were illuminated on one side of the cell, with a DC voltage application by an electrometer (ADC R8252). The photocurrent was recorded as a voltage drop through a serial resistor using a digital oscilloscope (Tektronics TDS 3044B). The transit time t_T was determined from the kink points of the transient photocurrent curves. The carrier mobility μ was calculated from equation 1, where d and V are the cell thickness and the applied voltage, respectively. Hole or electron mobilities were obtained when a positive or negative bias was applied to the illuminated electrode, respectively.

$$\mu = \frac{d^2}{Vt_T} \quad (1)$$

2.6. Photovoltaic effect measurement in films with planar electrodes

An ITO-coated substrate was patterned as shown in Figure S1 by concentrated hydrochloric acid. The channel width and length were 10 mm and 0.2 mm, respectively. The channel area was covered with a glass plate and the thickness between of the substrate and the covering glass plate was 4 μm. A high voltage exceeding 500 V was applied to the channel area for polarization of the FLC film. A UV light of Xe lump (300 W, Ushio Optical Modulex) was illuminated on the channel area through a UV filter. The photocurrent generated between the electrodes was measured by an electrometer (Keithley 6517A).

2.7. Dielectric measurement

A 2 μm-thick LC cell consisting of ITO-coated glass substrates (EHC, Japan) was fixed on a hot stage and connected to a LCZ meter (NF 2340). The frequency was scanned from 10 Hz to 1 MHz and the amplitude of the applied voltage signal was 0.2 V. In the polarized M* phase, the dielectric parameters were determined under the reverse bias of 1 V because the current-voltage characteristic indicated rectification because of the built-in potential produced by the spontaneous polarization.

2.8. Surface morphology study by atomic force microscope

The morphology of thin films of compound (*S*,*S*)-**1** was investigated by an atomic force microscopy (AFM). A sample was prepared on a glass substrate by spin-coating from cyclohexane solutions at room temperature. The AFM investigations were conducted under ambient conditions using a Multimode Nanoscope IV (Veeco Instruments, Santa Barbara) in tapping mode, using silicon cantilevers with a spring constant of 25 $N \cdot m^{-1}$ and a resonance frequency of 300 kHz (OMCL-AC240TS, Olympus). The scan rate was varied from 1 to 2 Hz.

3. Results and Discussion

3.1. Mesomorphic properties

Figure 1(a) shows DSC thermograms of compound (*S*,*S*)-**1**. Compound (*S*,*S*)-**1** exhibited a tilted ordered smectic phase below 101.2 °C and no crystallization peak was observed both in cooling and heating processes. The transition enthalpy was around 25 $J \cdot g^{-1}$ which was typical for a phase transition from an isotropic to an ordered smectic phase. The X-ray diffraction pattern (Figure 1(b)) reveals this mesophase has a layer structure and rectangular symmetry within the layers. The low angle peak at 2θ = 32.01 deg.

could be assigned to (001) diffraction plane and the layer spacing was 32.0 Å. An MM2 calculation reveals that the molecular length of compound (*S*,*S*)-**1** with an extended conformation is 45 Å. Comparing the molecular length of compound (*S*,*S*)-**1** with the layer spacing, the FLC molecules should be tilted in 45 deg. from the layer normal. From the high angle diffraction peaks, a rectangular lattice with lattice constants of 11.8 Å and 4.7 Å should be formed within the smectic layers. The high angle peaks indicate long-range order of molecular positions within the layers although it is disordered, compared to conventional molecular crystals because the high angle peaks are somewhat ambiguous. In the classical nomenclature, the M* phase is similar to a smectic K or H phase. This ordered smectic phase is denoted as M* phase. The assignment of the diffraction angles to diffraction indices is summarized in Table S1 in supporting information.

3.2. Nanostructure of spin-coated film of compound (S,S)-1

Fine structures on a nanometer scale of spin-coated thin films were studied by the atomic force microscopy. A cyclohexane solution of compound (*S*,*S*)-**1** was spun on a glass substrate. The spin-coated film was heated to 105 °C and cooled to room temperature. Figure 2(a) and (b) shows AFM topographic and phase images of the spin-coated film. A few domains with the size of several hundred nm were observed in both images. Within the domains, stripe patterns were formed and the width of the stripes was from 15 to 20 nm. The width of the stripes was slightly distributed. Periodical helical structures based on the molecular chirality are often formed in chiral supramolecular materials. However, the width of the stripes corresponded to around 5 smectic layers and much shorter than the standard value of the helical pitch of chiral smectic compounds. In this case, it should be plausible that the stripe pattern should be

originated from the polarization domains illustrated in Figure 2(c).

3.3. Polarization in the mesophase of compound (S,S)-1

The viscosity of the M* phase of compound (*S*,*S*)-**1** was too high and the speed of polarization inversion was slow. Under an application of a DC electric field on the order of 10^5 V·cm^{-1}, an optical texture change with partial polarization inversion occurred in several hours near the phase transition temperature to the isotropic phase. Consequently, spontaneous polarization in the M* phase could not be determined by a Sawyer-Tower method or a polarization inversion current measurement with a triangular wave application.

However, obvious difference between a non-polarized and polarized M* phases could be observed in a POM observation. Figure 3(a) shows POM textures in the non-polarized and polarized M* phase of compound (*S*,*S*)-**1** at 95 °C. The non-polarized M* phase was obtained when the sample was cooled from the isotropic phase to the M* phase without a DC bias. Fibrous grains with a length of several 10 μm were formed in the non-polarized M* phase. In contrast, fan-like domains typical of smectic phases were formed when the sample was cooled from the isotropic phase to the M* phase at 95 °C in the presence of a DC electric field of 1×10^5 V·cm^{-1}. The optical texture was retained after the removal of the DC bias and cooled to room temperature.

The accumulated charges in the polarized M* phase could be determined by thermally stimulated current (TSC) measurement [56], as shown in Figure 3(b). In a non-polarized phase, no remarkable increase in the TSC signal was observed at the transition from the M* phase to the isotropic phase. However, a current peak appeared in the TSC signals in the polarized M* samples. The direction of the TSC signal was

inverted by the inversion of the polarization of the M* phase. The integrals of the peaks in the positively and negatively polarized M* phases were around 3 $\mu C \cdot cm^{-2}$, indicating the polarization charges on the order of $\mu C \cdot cm^{-2}$ were accumulated in the polarized M* phase. It should be noted that these values should include not only spontaneous polarization but also space charges trapped in localized states and impurity.

In a cell with planar electrodes, a phase transition from the isotropic phase to the M* phase was induced by an application of a DC voltage under POM observation. Figure 4 shows POM textures in the cell with planar electrodes, described in Figure S1. Without a DC bias application, polydomain textures were formed as shown in Figure 4(a). The cell was heated to 105 °C and the sample transitioned to the isotropic phase, and only gap area changed to the M* phase when a DC bias over 500 V was applied (Figure 4(b)). The other area than the gap retained the isotropic phase. The phase transition temperature was raised by 2 K in the application of the electric field of 2.5×10^4 $V \cdot cm^{-1}$. This stabilization of the M* phase should be attributed to the interaction of the ferroelectric polarization with the electric field. From Figure 4(c) and (d), the axis of the gap area is parallel to the polarizer axis, indicating the FLC molecules should align parallel to the gap direction and polarization perpendicular to the gap direction should be induced.

3.4. Bulk photovoltaic effect in sandwich-type cells

Compound (*S*,*S*)-**1** exhibited the bulk photovoltaic effect in the polarized M* phase for white light illumination. Figure 5 exhibits current-voltage characteristics under illumination of white LED (20 $mW \cdot cm^{-2}$) at room temperature, using a 4 μm-thick sandwich-type cell. For polarization of the cells, a DC voltage of 40 V was applied to the cell in the isotropic phase and the cell was cooled to 50 °C retaining the DC voltage.

When a negative bias was applied to the front electrode, it was polarized positively. The current-voltage characteristics were measured by illuminating the front electrode.

As shown in Figure 5(a), the open-circuit voltage and short circuit-current were 1.12 V and 13.0 $\mu A \cdot cm^{-2}$ at room temperature, respectively. The fill factor reached 0.49, indicating efficient dissociation of excitons and effective inhibition of recombination of charge carriers. Total power conversion efficiency was 0.036 %. In the negatively polarized state, the polarity of the photovoltaic effect was inverted, as shown in Figure 5(b). The open-circuit voltage and the short circuit current decreased to 0.9 V and 3.6 $\mu A \cdot cm^{-2}$, respectively. The electron and hole mobilities were almost same although the electron generation efficiency was lower than that of the holes, as mentioned later. In the positively polarized state, the illuminated light was absorbed near the front electrode and the hole current contributed mainly to the total photocurrent, while the electron current was predominant in the photocurrent in the negatively polarized state. The open-circuit voltage, the short-circuit current, and the fill factor of compound (*S*,*S*)-**1** remarkably improved compared to compound **6** bearing lactate ester moieties [48]. The open-circuit voltage was 1.1 V in the positively polarized state, which was lower than the HOMO-LUMO gap of 2.4 eV for compound (*S*,*S*)-**1**, determined by UV-VIS absorption spectrum (Figure S2). But this value was higher than those of conventional junction-based photovoltaic cell.

It is noted that compound (*S*,*S*)-**1** indicated the bulk photovoltaic effect at room temperature unlike compound **6**. In the polarized smectic phase of compound **6**, the open-circuit voltage and short-circuit current remarkably decreased to 0.6 V and 0.8 $\mu A \cdot cm^{-2}$ at room temperature from 1.0 V and 6 $\mu A \cdot cm^{-2}$ at 70℃, respectively [48].

In the non-polarized state of compound (*S*,*S*)-**1**, no rectification character was

observed in the current-voltage characteristics, as shown in Figure S3(a). The behavior was photoconductor-like. In the non-polarized M* phase, excitation dissociation efficiency should be very low at the zero external bias and increase with the external electric field.

In the bulk photovoltaic effect, the open-circuit voltage should be proportional to the sample thickness. On the other hand, polarization is often relaxed in the bulk of soft crystals or ordered liquid crystal phases. In the bulk photovoltaic effect of the ferroelectric phase of compound **6** bearing monolactate moieties, the open-circuit voltage decreased in thick cells because of the polarization relaxation in the bulk, as reported previously [47]. The open-circuit voltage and the short circuit current of a 2 μm-thick cell were 1.0 V and 6 μAcm^{-2}, respectively, although these values decreased to 0.65 V and 2 μAcm^{-2} for a 4 μm-thick cell. Figure S3(b) exhibits the current-voltage characteristics in the polarized M* phase of samples with different thicknesses. The open-circuit voltage was 1.1 V and 0.9 V for 4 μm-thick and 2 μm-thick sample, respectively. The open-circuit voltage did not decrease with the cell thickness in the polarized M* phase of compound (*S*,*S*)-**1**. This result indicates that the polarization should be stabilized in the M* phase, due to the closer packing of double chiral side chains. The polarized state should be stabilized by inhibition of rotation of carbonyl groups in the lactate dimer side chains, due to steric hindrance of chiral moieties. Recently, Kishikawa and coworkers reported long-term stability of a polarized state in ferroelectric columnar LC phase of urea derivatives bearing chiral side chains. In the ferroelectric phase, a helical twisted columnar structure was formed to stabilize the polarized columnar structure by interaction between chiral side chains [58].

3.5. Carrier transport properties

Hole and electron mobilities in the M* phase were measured by the TOF technique. At 70 °C, non-dispersive photocurrent curves were obtained for holes and the hole mobility was determined to be 2×10^{-3} $cm^2 \cdot V^{-1}s^{-1}$ (Figure S4(a)). The hole mobility was independent of the electric field and the temperature. For electrons, the transient photocurrent curves were dispersive. However, the kink points were unambiguously determined in double logarithmic plots of the transient photocurrents and the electron mobility was estimated to be 2×10^{-3} $cm^2 \cdot V^{-1}s^{-1}$, which was independent of the electric field and the temperature (Figure S4(b)).

For dialkylterthiophene derivatives, alkynylterthiophene derivatives, and phenylterthiophene derivatives, the electronic carrier mobilities were on the order of 10^{-2} $cm^2 \cdot V^{-1}s^{-1}$ in the smectic phases which had long range orders within the smectic layers [27,28,31,59]. The hole and electron mobilities in the M* phase of (*S*,*S*)-**1** were one order magnitude lower than those in the ordered smectic phase of these compounds. This should be attributed to the bulky branched lactic acid moieties inhibiting closer packing of the π-conjugated units.

Figure 6 shows transient photocurrent curves for holes and electrons at room temperature. Even at room temperature, non-dispersive transient photocurrent curves were obtained and the hole and electron mobilities were retained to be over 10^{-3} $cm^2V^{-1}s^{-1}$. In most cases of π-conjugated ferroelectric liquid crystals, carrier transport characteristics degrades below room temperature because of carrier trapping in localized states and defects produced by contraction of the liquid crystal phases [39,40,46]. As indicated in Figure S4, the field-dependence of the hole and electron mobilities were weak, indicating small energetic and spatial disorders in the polarized

M* phase, assuming the disorder formalism [59,60]. As shown in Figure 3(a), large homogeneous domains with the size of several ten μm were formed in the polarized M* phase. The domain size was much larger than the sample thickness. Compared to the non-polarized state, defect density of the polarized domains should be suppressed to be low. Moreover, molecular dipoles aligned in the polarized M* phase not to broaden the density of states compared to the non-polarized M* phase in which molecular dipoles were not macroscopically oriented.

In compound **6** reported previously, non-dispersive transient photocurrent curves were obtained for hole while featureless dispersive ones were observed for electron at 70 °C [46]. The hole mobility was 1.3×10^{-3} $cm^2V^{-1}s^{-1}$ while the electron mobility could not be determined by the TOF method. As shown in Figure *S*6, transient photocurrents were dispersive both for holes and electrons at room temperature. The slope of the transient photocurrents in double logarithmic plots was around 1, indicating the presence of carrier traps in the bulk of compound **6**. This result indicates superior carrier transport property of compound (*S*,*S*)-**1** to that of compound **6** at room temperature. The bulkier dilactate side chains of (*S*,*S*)-**1** than the lactate moiety of compound **6** did not deteriorate the electronic charge carrier transport in the M* phase of compound (*S*,*S*)-**1**.

3.6. Dielectric relaxation spectra

Figure 7(a) exhibits dielectric relaxation spectra of compound (*S*,*S*)-**1** in the non-polarized M* phase at room temperature. Relaxation based on dipolar rotation around the molecular axis was observed around 10^5 Hz. The Goldstone mode as precession of the LC molecules around the helical axis should be remarkably slow, compared to conventional chiral smectic C phase of ferroelectric liquid crystals. The resonance frequency should be lower than 10 Hz because of the high viscosity of the M* phase. As

shown in Figure 7(b), the relaxation around 10^5 Hz in the non-polarized state shifted to 10^4 Hz in the polarized M* phase because of suppression of dipolar rotation around the molecular axis by the polarization field [61]. This relaxation should be attributed not to rotation but to flip-flap motion of polar moieties of the LC compound. The Goldston mode should also be suppressed in the polarized M* phase although the low frequency shift could not be clearly determined, due to the limitation of the apparatus. In the polarized M* phase, the relaxation of polarization was successfully suppressed to retain the internal electric field driving the bulk photovoltaic effect.

Figure S7 exhibits the dielectric relaxation spectra of compound **6** in non-polarized and polarized states at room temperature. The dielectric constant of compound **6** was six times larger than that of compound (*S*,*S*)-**1**. This smaller dielectric constant of (*S*,*S*)-**1** should be attributed to suppression of the flip-flap motion of dipoles of carbonyl groups which are fixed in the dilactate side chains. In compound **6**, the relaxation process based on the flip-flap motion of the dipoles was observed around 10^5 Hz although the lower frequency shift was not observed in the polarized state as observed in the polarized M* phase of compound (*S*,*S*)-**1**. These relaxation spectra indicates that fluctuation of dipoles in the dilactate side chains of compound (*S*,*S*)-**1** should be effectively suppressed compared to compound **6** bearing lactate ester moieties.

Assuming the relative dielectric constant, ε_r to be 20 in a DC field, the open-circuit voltage, expected V_{oc} was estimated. Accumulated charge density which was determined by the TSC measurement q is expressed as equation 2, where ε_0 and d is vacuum dielectric constant and sample thickness, respectively:

$$q = \varepsilon_0 \varepsilon_r \frac{V_{oc}}{d} \quad (2)$$

The expected V_{oc} is estimated to be 3.5×10^{2} V, using ε_0 of 8.85×10^{-12} Fm^{-1}, q of 3×10^{-6} $C\cdot cm^{-2}$, and d of 2×10^{-4} cm. The experimental V_{oc} was around 1 V, which was much lower than the expected value. If q was on the order of 10^{-8} $C\cdot cm^{-2}$, which was deduced from the spontaneous polarization in the SmC* phase of oligothiophene derivatives bearing lactate moieties, the expected V_{oc} should be several V. This discrepancy is attributed to the space charges injected into the ferroelectric liquid crystal layer. Polarization field promoted charge injection into the LC layer and some portion of the charge should be trapped in defects to form space charge which should be stabilized in the polarized medium, as reported in organic electrets [62]. The accumulated charge included not only polarization but also space charges formed in the LC layer. Moreover, the space charges also shielded the polarization field to reduce the potential difference between the electrodes.

3.7. Bulk photovoltaic effect in cells with planar electrodes

The bulk photovoltaic effect was also observed in cells with planar electrodes. The photovoltaic measurement in this alignment was often applied to the characterization of vacuum-deposited films and thin crystalline plates of inorganic ferroelectrics, such as bismuth ferrite and SnS. Figure 8 shows photocurrent as a function of the applied voltage for positively and negatively polarized state. The electrode-gap was 150 μm. Photocurrent dependent on the polarization was observed under zero external bias. The photocurrent flowed in the direction of polarization field, which was opposite to the polarity of the polling bias prior to the illumination. The inversion of the polling polarity resulted in the inversion of the photocurrent polarity as observed in a sandwich cell. The open-circuit voltage was 2.4 V for the both polarities. The open-circuit voltage is proportional to the distance between the electrodes in an ideal bulk photovoltaic

effect. The observed open-circuit voltage was comparable to the band gap of the ferroelectric liquid crystal. However, the open-circuit voltage should exceed 40 V from the open-circuit voltage 1.1 V in a sandwich cell with a thickness of 4 μm. The LC molecules oriented parallel to the planar electrodes although orientation of the molecular dipoles should relax in the area between the electrodes. Space charges originated from injected carriers should screen the internal electric field. The short-circuit current was 0.4 nA corresponding to 60 μAcm^{-2}, assuming the cross section of the electrode was 0.8 cm×20 nm. In most cases of bulk photovoltaic effects in inorganic and organic materials, current voltage characteristics have been linear although non-linear dependences were observed in the high field regions. This suggested inhomogeneous distribution of the polarization field in the channel area, due to space charges injected from the electrodes, Schottky barrier formation, or inhomogeneous relaxation of the polarization.

3.8. Bulk photovoltaic effect of (S,S)-1 doped with fullerene derivative

Figure 9 shows current-voltage characteristics in the M* phase of compound (*S*,*S*)-**1** doped with PCBM (8wt%). N-type PCBM microcrystals were segregated in the M* phase of p-type compound (*S*,*S*)-**1** to form bulk heterojunctions, as reported previously [46-49]. In contrast to previously reported terthiophene and quinquethiophene derivatives bearing lactic ester moieties, the bulk photovoltaic behavior was also observed even at room temperature. In the positively polarized state, the open-circuit voltage, short-circuit current, and fill factor were 0.95 V, 124 $\mu A \cdot cm^{-2}$, and 0.40, respectively. The power conversion efficiency was 0.24%. The photovoltaic effect was enhanced by doping of PCBM although the enhancement was not so remarkable as the case of the previously reported terthiophene and quinquethiophene derivatives bearing monolactate moieties [46-49]. The solubilities of fullerene

derivatives such as PCBM are higher in compound (*S*,*S*)-**1** than those in compound **6** bearing monolactate esters and PCBM molecules dispersed in the p-type LC domains should quench the photogenerated excitons. The lower dielectric constant of compound (*S*,*S*)-**1** than compound **6** should lower the exciton dissociation efficiency. The fill factor decreased in the doped sample, due to the increased structural disorder in the phase-separated M* phase. However, the fill factor remarkably improved from the value of 0.2 for compound **6** [48].

We also studied the photovoltaic effect of pure and PCBM-doped compound (*S*,*S*)-**1** for AM1.5 illumination (100 $mWcm^{-2}$), as shown in Figure S8. The results are summarized in Table S2. Both in the pure and PCBM-doped samples, the open circuit voltages were almost same as the cases of white LED illumination although short-circuit currents while the short circuit currents and fill factors were lower than the cases of white LED illumination. Compared to white LED, AM1.5 light contains longer wavelength component including in infrared light, resulting in lower power conversion efficiencies for AM1.5 illumination.

4. Conclusions

A π-conjugated FLC (*S*,*S*)-**1** bearing dilactate side chains was synthesized for an improved bulk photovoltaic effect. This compound exhibited a polarizable chiral ordered smectic phase below 101 °C. The polarization was estimated to be 3 $\mu C \cdot cm^{-2}$ by a TSC measurement. However, this value should include not only ferroelectric polarization but also space charges injected from the electrodes in the polling treatment. Compound (*S*,*S*)-**1** indicated the bulk photovoltaic effect without any electron acceptors even at room temperature with an open-circuit voltage of 1.1 V and the power conversion efficiency of 0.036%. The power conversion efficiency was enhanced by PCBM-doping in compound (*S*,*S*)-**1** to be 0.24%. The time-of-flight measurement

revealed that the effective carrier transport was retained at room temperature. The hole and electron mobilities exceeded 1×10^{-3} $cm^2V^{-1}s^{-1}$ at room temperature. Dielectric relaxation spectra revealed that the relaxation of dipolar fluctuation shifted from 10^5 Hz to 10^4 Hz in the polarized smectic phase, indicating suppression of thermal motion of the polar side chain. The double chiral structure of the dilactate side chains should suppress thermal fluctuation of the dipole moments of the carbonyl groups in the side chains. As a result, the polarized structure in the M* phase was stabilized and the increased intermolecular packing of the π-conjugated units should enhance the carrier transport at room temperature.

Acknowledgement

The author thanks Dr. Akinari Sonoda (AIST, Shikoku) for NMR measurements, Prof. Takafumi Kusunose (Kagawa Univ.) for DSC measurements, and Prof. Tomohiko Ishii (Kagawa Univ.) for X-ray diffraction analysis. This research was also supported by 'ARIM Japan' of the Ministry of Education, Culture, Sports, Science and Technology (MEXT), Japan (Grant No. JPMXP1222GA0004). This study was financially supported by a Grant-in-Aid for Scientific Research on Innovative Areas (Element-Block Polymers, no. 15H00753) from the Ministry of Education, Culture, Sports, Science and Technology (MEXT), a Grant-in-Aid for Scientific Research (B) (no.15H03797, 21H01904) from the Japan Society for the Promotion of Science (JSPS), the Toshiaki Ogasawara Memorial Foundation Science and Technology Grant, Naohiko Fukuoka Memorial Foundation, Iketani Science and Technology Foundation, and Japan Keirin Autorace Foundation (2022M-221).

REFERENCES

1 Matsuo H, Noguchi Y. Bulk photovoltaic effect in ferroelectrics. Jpn J Appl Phys. 2024; 63: 060101.

2 Shockley W, Queisser HJ. Detailed Balance Limit of Efficiency of p-n Junction Solar Cells. J Appl Phys. 1961; 32: 510-519.

3 Glass AM, von der Linde D, Negran T. J. High-voltage bulk photovoltaic effect and the photorefractive process in $LiNbO_3$. Appl Phys Lett. 1974; 25: 233-235.

4 Choi T, Lee S, Choi YJ, et al. Switchable Ferroelectric Diode and Photovoltaic Effect in BiFeO3. Science 2009; 324: 63-66.

5 Chang YR, Nanae R, Kitamura S, et al. Shift-Current Photovoltaics Based on a Non-Centrosymmetric Phase in In-Plane Ferroelectric SnS. Adv Mater. 2023; 35: 2301172.

6 Hatada H, Nakamura M, Sotome M, et al. Defect tolerant zero-bias topological photocurrent in a ferroelectric semiconductor. Proc Nat Acad Sci. 2020; 117: 20411-20415.

7 Yuan Y, Xiao Z, Yang B, et al. Arising applications of ferroelectric materials in photovoltaic devices. J Mater Chem A. 2014; 2: 6027-6041.

8 Dang Y, Tao X. Recent progress of bulk photovoltaic effect in acentric single crystals and optoelectronic devices. Matter. 2022; 5: 2659-2684.

9 Jiao S, Jiang H, Fan C, et al. Metal-free chiral molecular ferroelectric photovoltaics. Chem Eng J. 2023; 477: 146805.

10 Furukawa T. Ferroelectric properties of vinylidene fluoride copolymers Phase Transit. 1989; 18: 143-211.

11 Kobayashi K, Horiuchi S, Kumai R, et al. Electronic Ferroelectricity in a Molecular Crystal with Large Polarization Directing Antiparallel to Ionic Displacement. Phys Rev Lett. 2012; 108: 237601.

12 Horiuchi S, Tokura Y. Organic ferroelectrics. Nat Mater. 2008; 7: 357-366.

13 Sasabe H, Nakayama T, Kumazawa K, et al. Photovoltaic Effect in Poly(vinilydene fluoride). Polym J. 1981; 13: 967-973.

14 Sugita A, Suzuki K, Tasaka S. Ferroelectric properties of a triphenylene derivative with polar functional groups in the crystalline state. Phys Rev B Condens Matter Mater Phys. 2004; 69: 212201.

15 Nakamura M, Horiuchi S, Kagawa F, et al. Shift current photovoltaic effect in a ferroelectric charge-transfer complex. Nat Commun. 2017; 8: 281.

16 Clark NA, Lagerwall ST. Submicrosecond bistable electro-optic switching in liquid crystals. Appl Phys Lett. 1980; 36: 899-901.

17 Le KV, Takezoe H, Araoka F. Chiral Superstructure Mesophases of Achiral Bent-Shaped Molecules - Hierarchical Chirality Amplification and Physical Properties. Adv Mater. 2017; 29: 1602737.

18 Kishikawa K, Nakahara S, Nishikawa Y, et al. A Ferroelectrically Switchable Columnar Liquid Crystal Phase with Achiral Molecules: Superstructures and Properties of Liquid Crystalline Ureas. J Am Chem Soc. 2005; 127: 2565-2571.

19 Miyajima D, Araoka F, Takezoe H, et al. Ferroelectric Columnar Liquid Crystal Featuring Confined Polar Groups within Core-Shell Architecture. Science. 2012; 336: 209-213.

20 Nishikawa H, Shiroshita K, Higuchi H, et al. A Fluid Liquid-Crystal Material with Highly Polar Order. Adv Mater. 2017; 29: 1702354.

21 Kikuchi H, Matsukizono H, Iwamatsu K, et al. Fluid Layered Ferroelectrics with Global $C_{\infty v}$ Symmetry. Adv Sci. 2022; 9: 2202048.

22 Kato T, Yoshio M, Ichikawa T, et al. Transport of ions and electrons in nanostructured liquid crystals. Nat Rev Mater. 2017; 2: 17001.

23 Funahashi M. Solution-processable electronic and redox-active liquid crystals based on the design of side chains. Flex Print Electron. 2020; 5: 043001.

24 Adam D, Closs F, Frey T, et al. Transient photoconductivity in a discotic liquid crystal. Phys Rev Lett. 1993; 70: 457-460.

25 Würthner F, Saha-Möller CR, Fimmel B, et al. Perylene Bisimide Dye Assemblies as Archetype Functional Supramolecular Materials. Chem Rev. 2016; 116: 962-1052.

26 Funahashi M, Sonoda A. High electron mobility in a columnar phase of liquid-crystalline perylene tetracarboxylic bisimide bearing oligosiloxane chains. J Mater Chem. 2012; 22: 25190-25197.

27 Matsui A, Funahashi M, Tsuji T, et al. Hole Transport in Liquid-Crystalline Polymers with a Polysiloxane Backbone and a Phenylterthiophene Moiety in the Side Chain. Chem Eur J. 2010; 16: 13465-13472.

28 Funahashi M, Ishii T, Sonoda A. Temperature - Independent Hole Mobility of a Smectic Liquid-Crystalline Semiconductor based on Band-Like Conduction. ChemPhysChem. 2013; 14: 2750-2758.

29 Aldred MP, Contoret AEA, Farrar SR, et al. A Full Color Electroluminescence Device and Patterned Photoalignment Using Light Emitting Liquid Crystal. Adv Mater. 2005; 17: 1368-1372.

30 Pisula W, Menon A, Stepputat M, et al. A Zone Casting Technique for Device Fabrication of Field-Effect Transistors Based on Discotic Hexa-peri-Hexabenzocoronene. Adv Mater. 2005; 17: 684-689.

31 Funahashi M, Zhang F, Tamaoki N. High ambipolar mobility in highly ordered smectic phase of dialkylphenylterthiophene derivative that can be applied to solution-processed organic field effect transistors. Adv Mater. 2007; 19: 353-358.

32 Iino H, Usui T, Hanna J. Liquid crystals for organic thin-film transistors. Nat Commun. 2015; 6: 6828.

33 Schmidt-Mende L, Fechtenkötter A, Müllen K, et al. Self-Organized Discotic Liquid Crystals for High-Efficiency Organic Photovoltaics. Science. 2001; 293: 1119-1122.

34 Hori T, Miyake Y, Yamasaki N, et al. Solution Processable Organic Solar Cell Based on Bulk Heterojunction Utilizing Phthalocyanine Derivative. Appl Phys Express. 2010; 3: 101602.

35 Garcia-Iglesias M, de Waal BFM, Gorbunov AV, et al. Versatile method for the preparation of ferroelectric supramolecular materials via radical end-functionalization of vinylidene fluoride oligomers. J Am Chem Soc. 2016; 138: 6217-6223.

36 Gorbunov AV, Iglesias MG, Guilleme J, et al. Ferroelectric self-assembled molecular materials showing both rectifying and switchable conductivity. Sci Adv. 2017; 3: e1701017.

37 Anetai H, Wada Y, Takeda T, et al. Fluorescent Ferro-electrics of Hydrogen-Bonded Pyrene Derivatives. J Phys Chem Lett. 2015; 6: 1813-1818.

38 Sambe K, Takeda T, Hoshino N, et al. Carrier Transport Switching of Ferroelectric BTBT Derivative. J Am Chem Soc. 2024; 146: 8557-8566.

39 Funatsu Y, Sonoda A, Funahashi M. Ferroelectric liquid-crystalline semiconductors based on a phenylterthiophene skeleton: Effect of introduction

of oligosiloxane moieties and photovoltaic effect. J Mater Chem C. 2015; 3: 1982-1993.

40 Seki A, Funatsu Y, Funahashi M. Anomalous photovoltaic effect based on molecular chirality: Influence of enantiomeric purity on the photocurrent response in π-conjugated ferroelectric liquid crystals. Phys Chem Chem Phys. 2017; 19: 16446-16455.

41 Seki A, Funahashi M. Chiral photovoltaic effect in an ordered smectic phase of a phenylterthiophene derivative. Org Electron. 2018; 62: 311-319.

42 Seki A, Yoshio M, Mori Y, et al. Ferroelectric Liquid-Crystalline Binary Mixtures Based on Achiral and Chiral Trifluoromethylphenylterthiophenes. ACS Appl Mater Interfaces. 2020; 12: 53029-53038.

43 Mori Y, Funahashi M. Bulk photovoltaic effect in organic binary systems consisting of a ferroelectric liquid crystalline semiconductor and fullerene derivatives. Org Electron. 2020; 87: 105962.

44 Zhang C, Nakano K, Nakamura M, et al. Noncentrosymmetric Columnar Liquid Crystals with the Bulk Photovoltaic Effect for Organic Photodetectors. J Am Chem Soc. 2020; 142: 3326-3330.

45 Lehmann M, Baumann M, Lambov M, et al. Parallel Polar Dimers in the Columnar Self-Assembly of Umbrella-Shaped Subphthalocyanine Mesogens. Adv Funct Mater. 2021; 38: 2104217.

46 Murad A, Baron E, Feneberg M, et al. Polarity in liquid crystals formed by self-assembled umbrella-shaped subphthalocyanine mesogens. ACS Appl Mater Interfaces. 2024; 16: 25025-25032.

47 Funahashi M, Mori Y. Linearly polarized electroluminescence device in which the polarized plane can be rotated electrically using a chiral liquid crystalline semiconductor. Mater Chem Front. 2020; 4: 2137-2148.

48 Funahashi M. High open-circuit voltage in the bulk photovoltaic effect for the chiral smectic crystal phase of a double chiral ferroelectric liquid crystal doped with a fullerene derivative. Mater Chem Front. 2021; 5: 8265-8274.

49 Matoba Y, Uemura S, Funahashi M. Diastereomeric effect on bulk photovoltaic property and polarized electroluminescence in ferroelectric liquid crystals containing an extended π-conjugated unit. Bull Chem Soc Jpn. 2023; 96: 247-256.

50 Funahashi M. Bulk photovoltaic effect in ferroelectric liquid crystals comprising of quinquethiophene and lactic ester units. Org Electron. 2023; 122: 106911.

51 Funahashi M, Sonoda A. Electron transport characteristics in nanosegregated columnar phases of perylene tetracarboxylic bisimide derivatives bearing oligosiloxane chains. Phys Chem Chem Phys. 2014; 16: 7754-7763.

52 Funahashi M, Zhang F, Tamaoki N, et al. Ambipolar transport in the smectic E phase of 2-propyl-5’’- hexynylterthiophene derivative over a wide temperature range. ChemPhysChem. 2008; 9: 1465-1473.

53 Bubnov A, Cigl M, Mironov S, et al. The correlations between the molecular core structure and mesomorphic behaviour for chiral liquid crystals with several (*S*)-lactate groups. J Mol Liq. 2023; 387: 122590.

54 Ishiyama T, Murata M, Miyaura N. Palladium(0)-Catalyzed Cross-Coupling Reaction of Alkoxydiboron with Haloarenes: A Direct Procedure for Arylboronic Esters. J Org Chem. 1995; 60: 7508-7510.

55 Miyaura N, Yanagi T, Suzuki A. The Palladium-Catalyzed Cross-Coupling Reaction of Phenylboronic Acid with Haloarenes in the Presence of Bases. Synth Commun. 1981; 11: 513-519.

56 van Turnhout J. Thermally Stimulated Discharge of Polymer Electrets. Polym J. 1971; 2: 173-191.

57 Funahashi M. Time-of-flight method for determining the drift mobility in organic semiconductors. Organic Semiconductors for Optoelectronics, edited by Hiroyoshi Naito, Wiley interscience 2021.

58 Akiyama A, Jido K, Kohri M, et al. Generation of Axially Polar Ferroelectricity in a Columnar Liquid Crystal Phase by Introducing Chirality. Adv Electron Mater. 2020; 6: 2000201.

59 Funahashi M, Zhang F, Tamaoki N, et al. Ambipolar transport in the highly ordered smectic phase of 2-alkyl-5"-alkynyl- terthiophene derivative in a wide temperature range. ChemPhysChem. 2008; 9: 1465-1473.

60 Bässler H. Charge transport in disordered organic photoconductors - a Monte Carlo simulation study. Phys Stat Solid B. 1993; 175: 15-56.

61 Vallerien SU, Kremer F, Kapitza H, et al. Field dependent soft and Goldstone mode in a ferroelectric liquid crystal as studied by dielectric spectroscopy. Phys Lett. 1989; 138: 219-222.

62 Ghosh A, Yoshida M, Suemori K, et al. Soft chromophore featured liquid porphyrins and their utilization toward liquid electret applications. Nat Commun. 2019; 10: 4210.

Table of Content

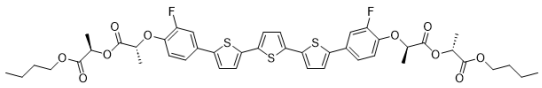

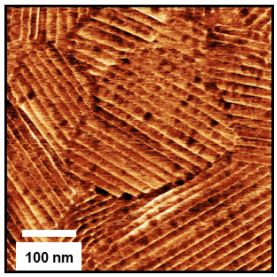

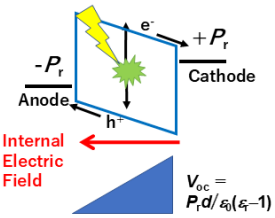

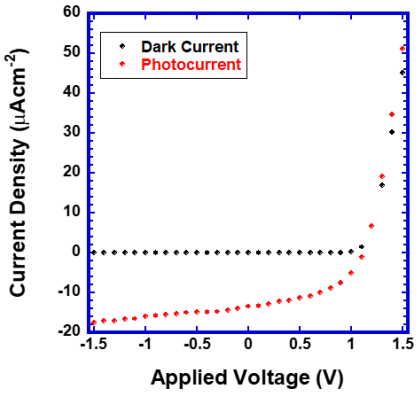

Graphical Abstarct

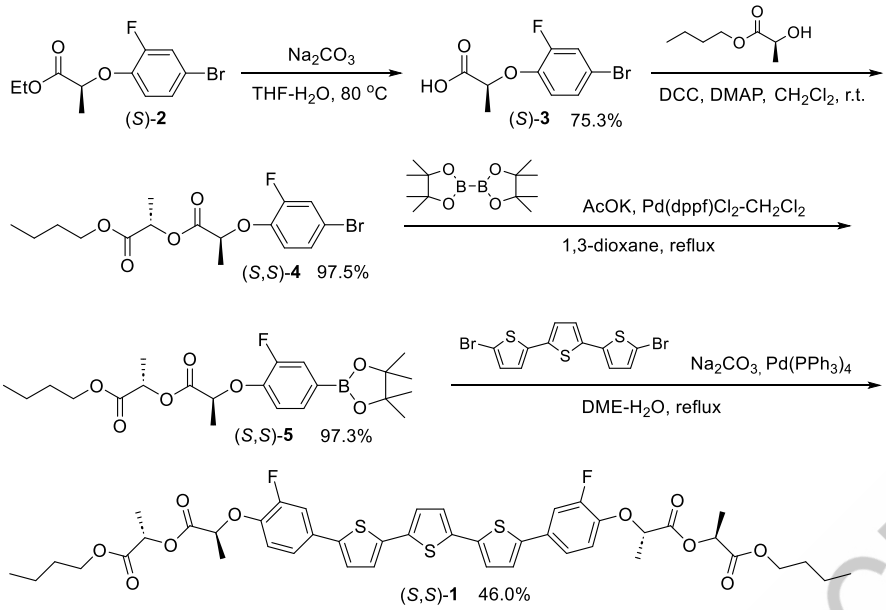

Scheme 1. Synthetic route of FLC (*S*,*S*)-**1** bearing lactide dimers in the side chains.

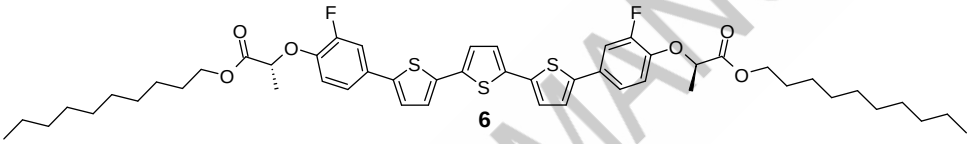

Scheme 2. Molecular structure of compound **6** bearing lactate ester moieties.

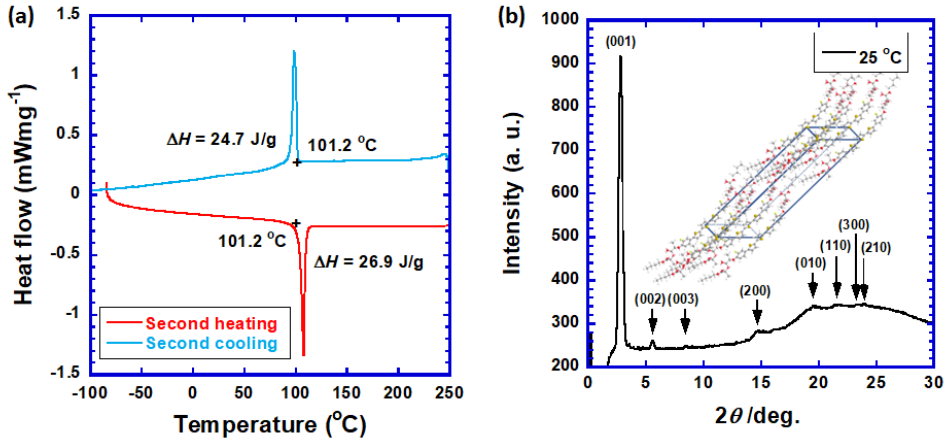

Figure 1. (a) DSC thermograms of compound (*S*,*S*)-**1** at cooling and heating rates of 10 K·min^{-1}. (b) X-ray diffraction pattern of compound (*S*,*S*)-**1** in an ordered smectic phase

at room temperature. The inset indicates a schematic illustration of molecular packing in the smectic phase.

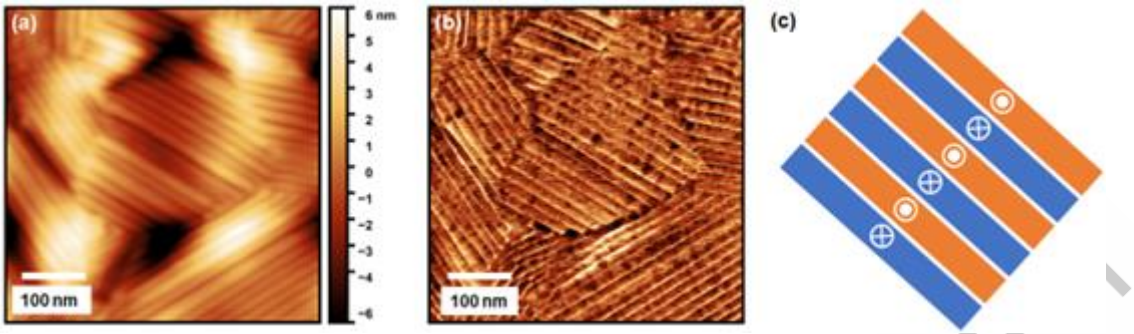

Figure 2. (a) AFM topographic and (b) phase images of a spin-coated film of compound (*S*,*S*)-**1**. (c) Schematic for polarized domains in the stripe pattern observed in the AFM images. Symbols ◉ and ⊗ are direction of polarization of the domains.

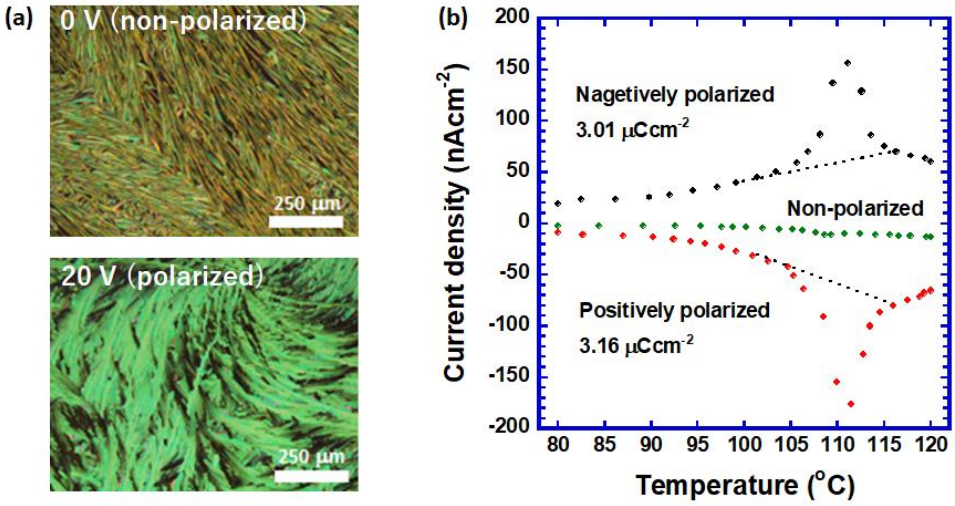

Figure 3. (a) Polarizing optical micrographic textures in the non-polarized and polarized M* phase of compound (*S*,*S*)-**1** at 95°C. The sample thickness was 2 μm. The upper and lower images show the textures formed without a DC bias for a non-polarized M* phase and under the application of the DC bias of 20 V for a polarized M* phase, respectively. (b) Thermally stimulated current as a function of the temperature for compound (*S*,*S*)-**1**.

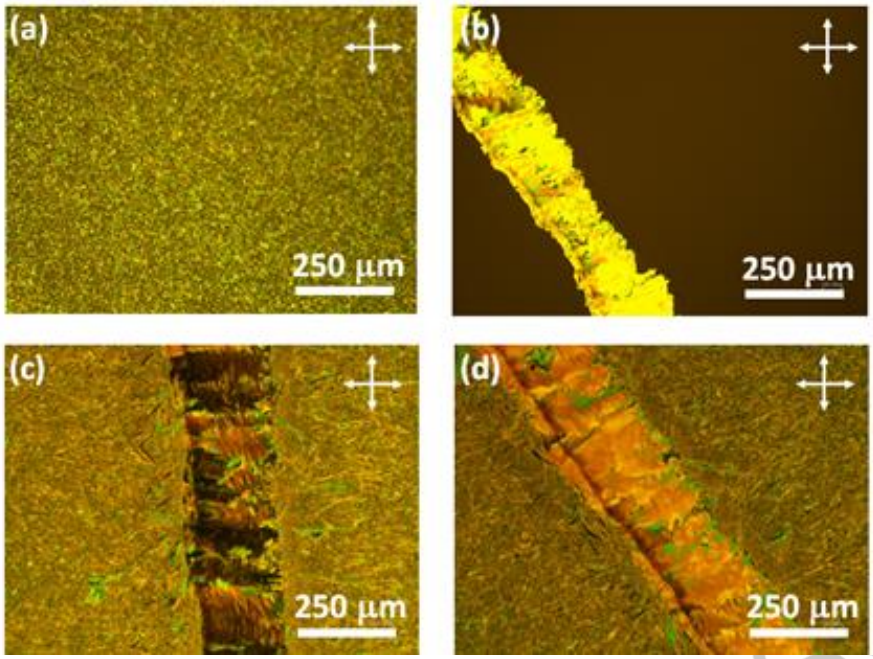

Figure 4. Polarizing micrographic textures of compound (*S*,*S*)-**1** in a cell with planar electrodes with a gap of 0.2 mm at (a) room temperature with no DC bias, (b) 105 °C with a DC bias of 700 V. POM images of the gap area of the sample at room temperature with the polarizer axis (c) parallel and (d) tilted to the gap direction.

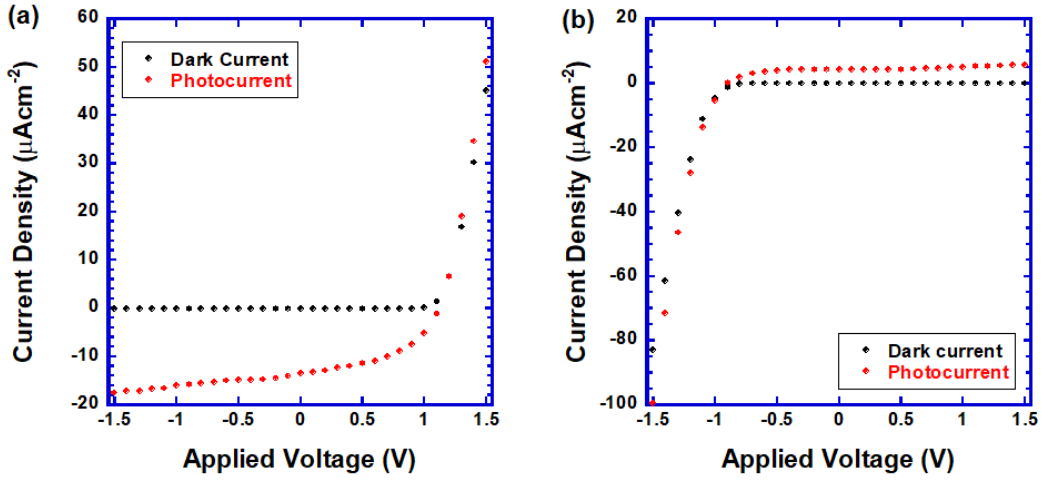

Figure 5. Current-voltage characteristics in the M* phase of compound (*S*,*S*)-**1** polarized (a) positively and (b) negatively when white light (LED, 20 mW·cm^{-2}) was illuminated at room temperature. The sample thickness was 4 µm.

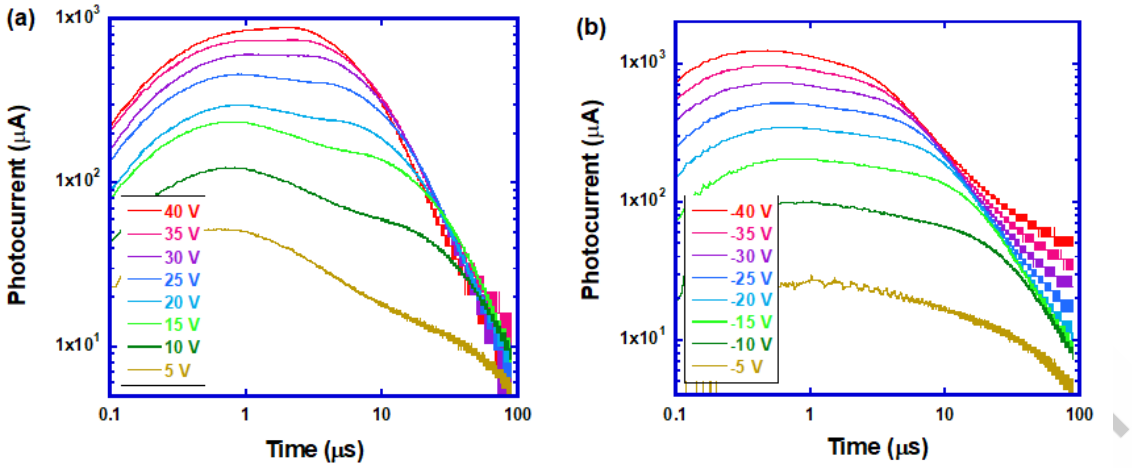

Figure 6. Transient photocurrent curves for (a) holes and (b) electrons in the M* phase of compound (*S*,*S*)-**1** at 20 °C. The excitation light was THG of a Nd:YAG laser (wavelength = 356 nm) and the sample thickness was 4 μm.

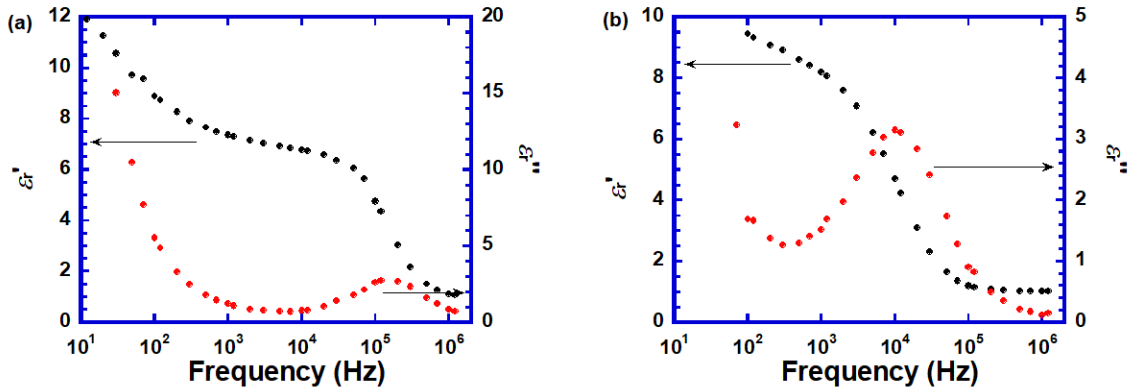

Figure 7. Dielectric relaxation spectra in (a) the non-polarized and (b) polarized M* phase of compound (*S*,*S*)-**1** at room temperature.

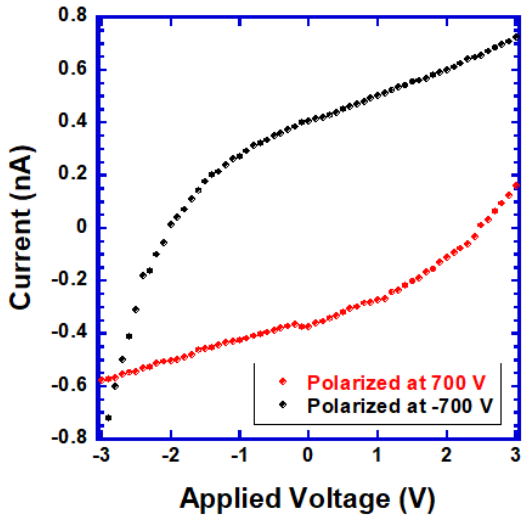

Figure 8. Current-voltage characteristics of compound (*S*,*S*)-**1** in a cell with planar electrodes at 70 °C.

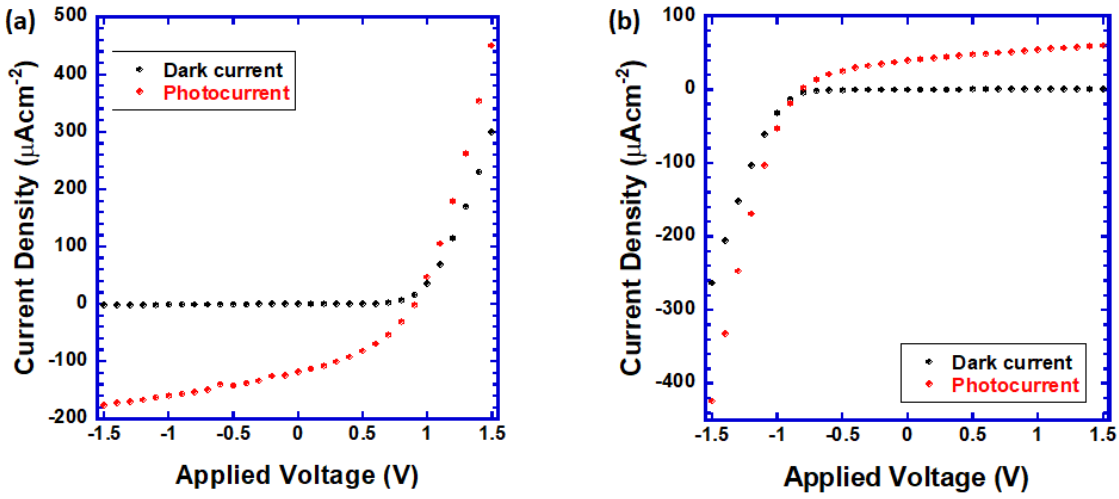

Figure 9. Current-voltage characteristics in the M* phase of compound (*S*,*S*)-**1** doped with PCBM (8 wt%), with (a) positive and (b) negative polarization when white light (LED, 20 mW·cm^{-2}) was illuminated at room temperature. The sample thickness was 4 μm.

Statement of Novelty

We report room-temperature bulk photovoltaic effect of a ferroelectric liquid crystal based on diphenylterthiophene bearing dilactate side chains. Polarized structure was stabilized to retain good carrier transport at room temperature.

Supporting information

Room-temperature bulk photovoltaic effect in a terthiophene-based ferroelectric liquid crystal bearing dilactate side chains

Masahiro Funahashi*[1,2,5], Yasuko Koshiba[1,2], Shohei Horike[1,2,3], and Shinobu Uemura[4,5]

[1]Department of Chemical Science and Engineering, Graduate School of Engineering, Kobe University

[2]Research Center for Membrane and Film technology, Kobe University

[3]Center for Environmental Management, Kobe University

1-1 Rokkodai, Nada-ku, Kobe, Hyogo 657-8501, Japan

[4]Program in Advanced Materials Science, Faculty of Engineering and Design, Kagawa University

2217-20 Hayashi-cho, Takamatsu, Kagawa 761-0396, Japan

[5]Health and Medical Research Institute, National Institute of Advanced Industrial Science and Technology

2217-14 Hayashi-cho, Takamatsu, Kagawa 761-0395, Japan

Synthesis of Materials

General

All reactions were performed under nitrogen atmosphere in a well-dried three-necked flask equipped with a magnetic stirring bar. Organic solvents and other chemicals were commercially available from Sigma-Aldrich, Tokyo Chemical Industry, Kanto Chemicals, and Fujifilm Wako Chemicals. Silica gel was purchased from Kanto Chemicals. All purchased materials were used as received. ^{1}H and ^{13}C nuclear magnetic resonance (NMR) spectra were recorded on a Varian UNITY INOVA 400NB spectrometer. Infrared absorption spectra were determined using Perkin-Elmer Spectrum 3 FTIR.

Synthetic procedures and spectral data

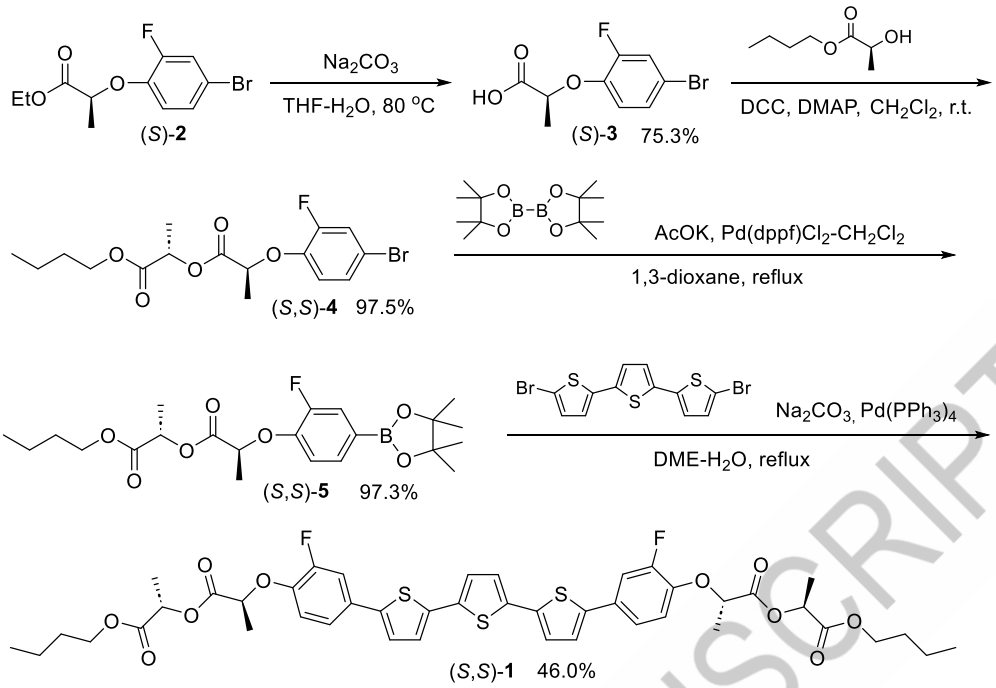

Scheme S1 Synthetic route of compounds (*S*,*S*)-**1**

(*S*)-2-(4-bromo-2-fluorophenoxy)propanoic acid ((*S*)-3)

Ethyl (*S*)-2-(4-bromo-2-fluorophenoxy)propanoate ((*S*)-**2**) (23.81 g, 0.081 mol) was dissolved in ethanol (100 ml). An aqueous solution of sodium carbonate (10.80 g, 0.102 mol/ water 50 ml) was added to the solution and it was stirred at 80 °C for 3 hours. After cooling the reaction mixture to room temperature, and it was neutralized by dilute hydrochloric acid. The resultant solution was extracted by ethyl acetate. The extract was dried over sodium sulfate and the solvent was evaporated. The residual solids were recrystallized from *n*-hexane. White needles (17.81 g) were obtained in the yield of 75.3 %.

^{1}H-NMR (400 MHz, $CDCl_3$) : δ = 7.27 (1H, dt, J = 10.4, 2.4 Hz), 7.18 (1H, ddd, J = 9.2, 4.0, 2.4 Hz), 6.85 (1H, dt, J = 9.2, 2.4 Hz), 4.78 (1H, quartet, J 6.8 Hz), 1.68 (3H, d, J = 6.8 Hz) ppm.

FT-IR (ATR): ν = 2990.0, 2939.0, 1709.5, 1677.9, 1606.0, 1583.3, 1493.5, 1451.7, 1440.8, 1411.5, 1397.8, 1372.2, 1327.8, 1304.2, 1280.1, 1264.2, 1251.6, 1231.2, 1200.4, 1136.5, 1103.8, 1072.5, 1044.8, 950.0, 900.6, 864.3, 832.5, 794.3, 786.2, 636.1, 603.9, 575.9, 517.1, 499.3, 449.9 cm^{-1}.

Chemical Formula: $C_{11}H_{12}BrFO_3$, Exact Mass: 290.00, Molecular Weight: 291.12 m/z: 290.00 (100.0%), 291.99 (97.3%), 291.00 (12.1%), 293.00 (11.9%), 292.00 (1.3%), 294.00 (1.3%) Elemental Analysis: C, 45.38; H, 4.16; Br, 27.45; F, 6.53; O, 16.49. Found: C, 41.17; H, 3.13.

(*S*)-1-butoxy-1-oxopropan-2-yl (*S*)-2-(4-bromo-2-fluorophenoxy)propanoate ((*S*,*S*)-4)

Compound (*S*)-**3** (10.01 g, 38 mmol) and (*S*)-butyl lactate (6.08 g, 41 mmol) were dissolved in dichloromethane (120 ml). *N*,*N*'-dicyclohexylcarbodiimide (8.22 g, 40 mmol) was dissolved in dichloromethane (30 ml) and it was added dropwise to the solution of compound (*S*)-**3** and (*S*)-butyl lactate at 0 °C. After stirring the reaction mixture at room temperature for 1 hour, the crystals of dicylohexyl urea were filtered off and the filtrate was concentrated. The residual oil was purified by a silicagel column chromatography (elutant: dichloromethane). Colorless oil (14.40 g, 37 mol) was obtained in the yield of 97 %.

^{1}H-NMR (400 MHz, $CDCl_3$) : δ = 7.25 (1H, dd, J = 10.4, 2.4 Hz), 7.16 (1H, ddd, J = 8.4, 2.4, 1.6 Hz), 6.88 (1H, t, J = 8.4 Hz), 5.14 (1H, quartet, J = 7.2 Hz), 4.79 (1H, quartet, J = 6.4 Hz), 4.13 (2H, t, J = 6.4 Hz), 1.71 (3H, d, J 6.4 Hz), 1.46-1.66 (3H, m), 1.51 (3H, d, J = 7.2 Hz), 1.35 (2H, sextet, J = 6.8 Hz), 0.93 (3H, t, J = 6.8 Hz) ppm.

FT-IR (ATR): ν = 2961.3, 2875.0, 1744.3, 1583.5, 1497.2, 1455.7, 1409.7, 1378.4, 1347.6, 1302.0, 1266.0, 1184.9, 1134.0, 1092.0, 1046.5, 951.8, 864.9, 800.9, 784.6, 756.8, 637.8, 574.5, 503.2, 449.7, 385.3 cm^{-1}.

Chemical Formula: $C_{16}H_{20}BrFO_5$, Exact Mass: 390.05, Molecular Weight: 391.23

m/z: 390.05 (100.0%), 392.05 (99.7%), 391.05 (17.7%), 393.05 (17.2%), 394.05 (2.4%)

Elemental Analysis: C, 49.12; H, 5.15; Br, 20.42; F, 4.86; O, 20.45. Found: C, 48.66; H, 5.01.

(*S*)-1-butoxy-1-oxopropan-2-yl (*S*)-2-(2-fluoro-4-(4,4,5,5-tetramethyl-1,3,2-dioxaborolan-2-yl) phenoxy)propanoate ((*S*,*S*)-5)

Compound (*S*,*S*)-**4** (10.04 g, 25.7 mmol), potassium acetate (4.51 g, 55 mmol) and bis(pinacolato)diboron (11.00 g, 43 mmol) were dissolved in 1,3-dioxane (200 ml). To the suspension, [1,1'-bis(diphenylphosphino)ferrocene]palladium(II) Dichloride Dichloromethane Adduct (53.9 mg, 0.066 mmol) was added and the reaction mixture was refluxed for 5 hours. After cooling the mixture to room temperature, the insoluble precipitates were filtered off. The filtrate was dissolved in ethyl acetate and washed with water and brine. The extract was dried over sodium sulfate and concentrated. The residual oil was purified by a silcagel column chromatography (elutant: dichloromethane). Colorless oil (10.95 g, 25.0 mmol) was obtained in the yield of 97.3 %.

^{1}H-NMR (400 MHz, $CDCl_3$) : δ = 7.51 (1H, d, J = 8.4 Hz), 7.48 (1H, d, J = 6.8 Hz), 6.93 (1H, t, J = 8.4 Hz), 5.15 (1H, quartet, J = 7.2 Hz), 4.89 (1H, quartet, J = 7.2 Hz), 4.12 (2H, t, J = 6.8 Hz), 1.72 (3H, d, J = 6.8 Hz), 1.59 (2H, quintet, J = 6.8 Hz), 1.51 (3H, d, J = 6.8 Hz), 1.38-1.32 (2H, m), 1.32 (12H, s), 0.92 (3H, t, J = 7.2 Hz) ppm.

FT-IR (ATR): ν = 2977.8, 1749.1, 1604.5, 1571.8, 1487.8, 1456.7, 1396.9, 1360.4, 1319.0, 1275.2, 1239.8, 1211.6, 1181.6, 1123.6, 1087.0, 1050.8, 1013.4, 961.7, 859.6, 848.9, 830.7, 735.2, 670.2, 654.5, 623.3, 578.2, 505.2, 448.1, 414.3, 397.9 cm^{-1}.

Chemical Formula: $C_{22}H_{32}BFO_7$, Exact Mass: 438.22, Molecular Weight: 438.30

m/z: 438.22 (100.0%), 439.23 (25.5%), 437.23 (24.8%), 438.23 (6.1%), 440.23 (4.4%)

Elemental Analysis: C, 60.29; H, 7.36; B, 2.47; F, 4.33; O, 25.55. Found: C, 57.83; H, 7.48.

Bis((*S*)-1-butoxy-1-oxopropan-2-yl) 2,2'-(([2,2':5',2''-terthiophene]-5,5''-diylbis(2-fluoro-4,1-phenylene))bis(oxy))(2*S*,2'*S*)-dipropionate ((*S*,*S*)-1)

Compound (*S*,*S*)-**5** (2.73 g, 6.2 mmol), 5,5”-dibromo-2,2’:5’,2”-terthiophene (0.98 g, 2.4 mmol), and tetrakis(triphenylphosphine) palladium (0) (17.2 mg, 0.015 mmol) were dissolved in dimethoxyethane (50 ml). An aqueous solution (20 ml) of sodium carbonate (0.67 g, 6.3 mmol) was added to the reaction mixture. It was refluxed for 30 minutes and cooled to room temperature. Water was added to the reaction mixture and resultant precipitates were filtered off. The precipitates were washed with water and methanol. The residual solids were purified by a silicagel column chromatography (elutant: dichloromethane). The crude product was dissolved in dichloromethane and the solution was poured into methanol. The yellow precipitates were filtered and recrystallized from a mixed solvent of ethyl acetate and *n*-hexane. Pale yellow needles (0.94 g, 1.1 mmol) were obtained in the yield of 46 %.

^{1}H-NMR (400 MHz, $CDCl_3$) : δ = 7.33 (2H, dd, J = 12.4, 2.4 Hz), 7.26 (2H, ddd, J = 8.4, 2.4, 1.2 Hz), 7.12 (4H, s), 7.10 (2H, s), 7.00 (2H, t, J 8.4 Hz), 5.17 (2H, quartet, J = 7.2 Hz), 4.87 (2H, quartet, J = 7.2 Hz), 4.14 (4H, t, J = 7.2 Hz), 1.74 (6H, d, J = 7.2 Hz),

1.61 (4H, quintet, J = 7.2 Hz), 1.53 (6H, d, J = 7.2 Hz), 1.36 (4H, sextet, J = 7.2 Hz), 0.92 (6H, t, J = 7.2 Hz) ppm.

FT-IR (ATR): ν = 2956.4, 1749.0, 1578.8, 1526.7, 1493.7, 1452.9, 1429.6, 1348.0, 1300.0, 1285.5, 1268.8, 1202.7, 1128.9, 1097.3, 1042.9, 954.7, 865.2, 837.2, 821.9, 789.9, 624.4, 484.8, 442.9, 397.8 cm^{-1}.

Chemical Formula: $C_{44}H_{46}F_2O_{10}S_3$, Exact Mass: 868.22, Molecular Weight: 869.02

m/z: 868.22 (100.0%), 869.23 (48.5%), 870.22 (14.6%), 870.23 (13.6%), 871.22 (6.7%), 871.23 (3.0%), 869.22 (2.4%), 872.22 (1.9%)

Elemental Analysis: C, 60.81; H, 5.34; F, 4.37; O, 18.41; S, 11.07. Found: C, 60.65; H, 5.36.

Structure of a substrate with planar electrodes

On a substrate with planar electrodes (Figure S1), a small amount of compound (*S*,*S*)-**1** was put and the substrate was heated to 120℃. A cover glass slide was put on the melt compound and the sample was cooled to room temperature.

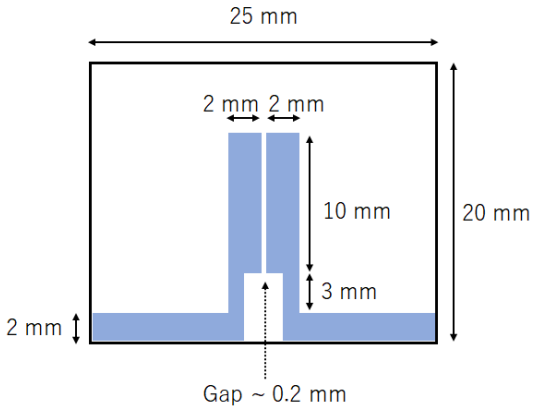

Figure S1 Schematic for a patterned ITO substrate with planar electrodes.

X-ray diffraction data of compound (*S*,*S*)-1

X-ray diffraction data of compound (*S*,*S*)-1 are summarized in Table S1. The FLC molecules are self-organized into a layer structure in which the layer spacing is 32.0 Å. The FLC molecules tilt in 45 deg. from the layer normal. Within the layers, the FLC molecules are arranged in a rectangular symmetry with the lattice constants of 11.8 Å and 4.7 Å.

Table S1 Diffraction peaks, assigned diffraction plane indices and d-spacings of compound (*S*,*S*)-**1**.

2θ/deg.	d_{exp} /Å	*h*	*k*	*l*	d_{calc} /Å
2.76	32.01	0	0	1	32.00
5.50	16.07	0	0	2	16.00
8.40	10.53	0	0	3	10.67
11.20	7.90	0	0	4	8.00
15.22	5.82	2	0	0	5.90
19.16	4.63	0	1	0	4.70
20.11	4.42	1	1	0	4.37
22.11	4.02	3	0	0	3.93
24.17	3.68	2	1	0	3.68

Photoconductivity in the non-polarized M* phase and thickness-dependence on bulk photovoltaic effect in the polarized M* phase

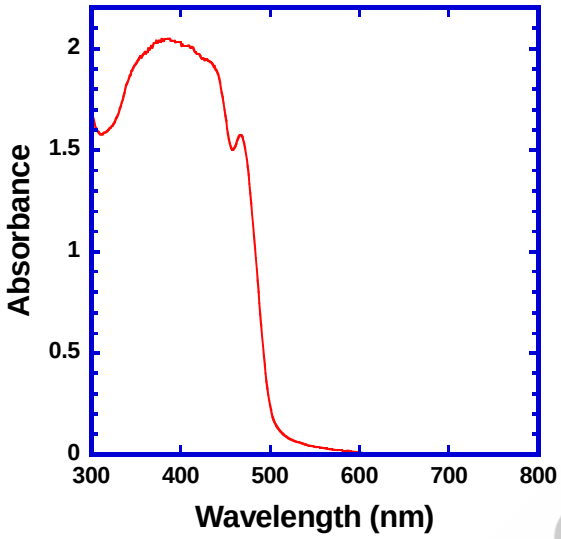

Figure S2 UV-VIS absorption spectrum of compound (*S*,*S*)-**1** in a thin film state (thickness ~ 1 μm)

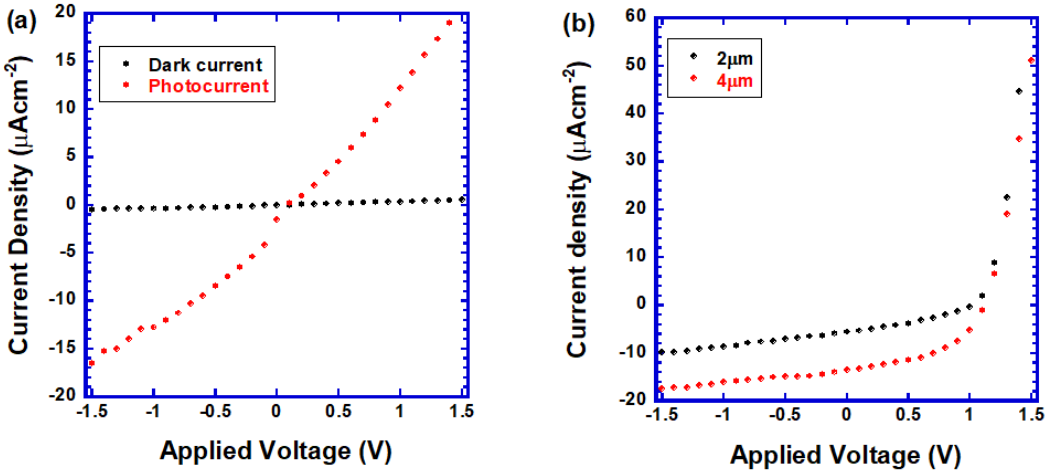

Figure S3 (a) Current-voltage characteristic in the non-polarized M* phase for white light (LED, 20 mW·cm^{-2}) illumination at room temperature. (b) Current-voltage characteristic in the polarized M* phase for white light (LED, 20 mW·cm^{-2}) illumination at room temperature for samples with different thicknesses.

Carrier transport in the M* phase of compounds (*S*,*S*)-1 and 6

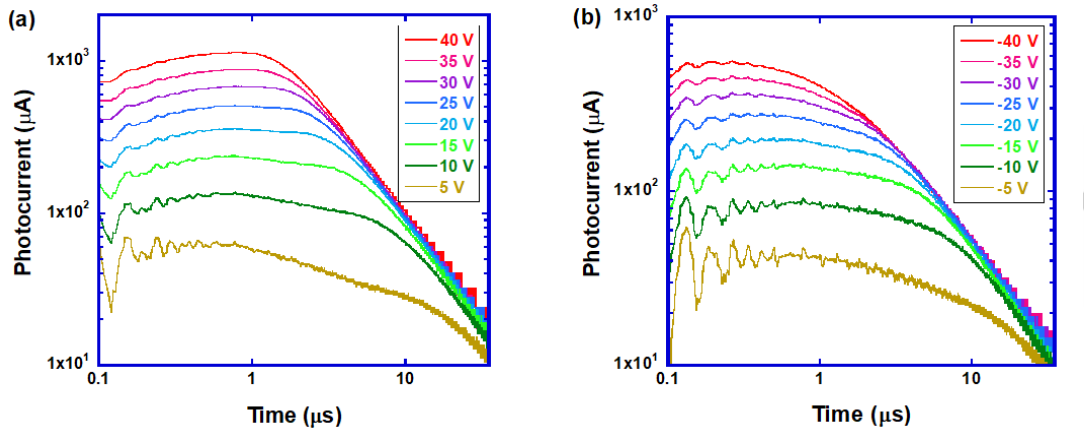

Figure S4 Transient photocurrent curves for (a) holes and (b) electrons in the M* phase of compound (*S*,*S*)-**1** at 70℃. The excitation light was THG of a Nd:YAG laser (wavelength = 356 nm) and the sample thickness was 4 μm.

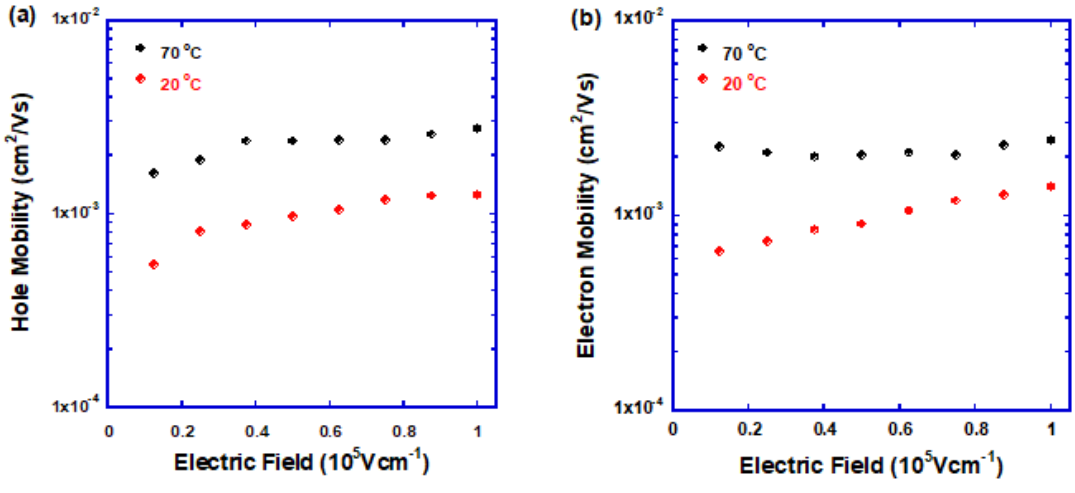

Figure S5 Carrier mobilities as a function of the electric field for (a) holes and (b) electrons in the polarized M* phase of compound (*S*,*S*)-**1** at 70℃ and 20℃.

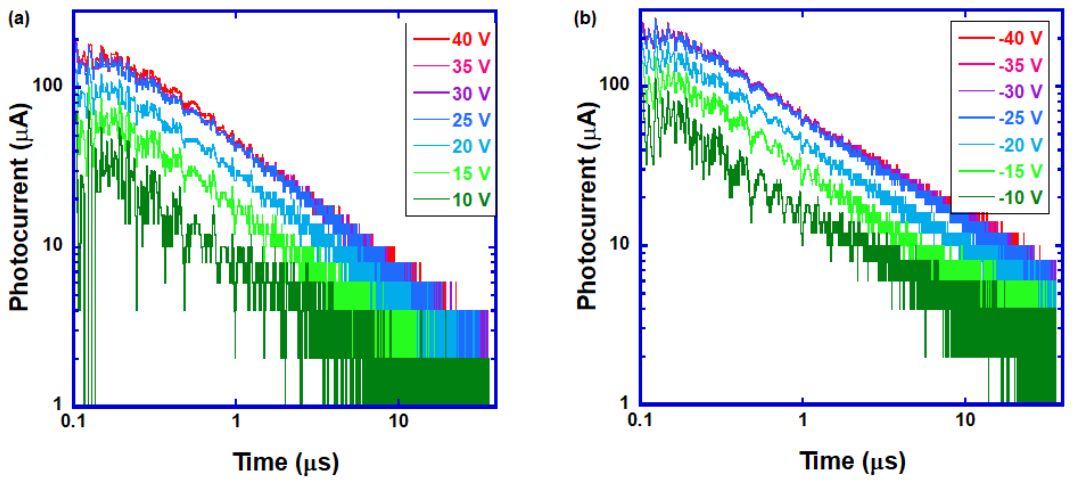

Figure S6 Transient photocurrent curves for (a) holes and (b) electrons in the polarized smectic phase of compound **6** at room temperature. The excitation light was THG of a Nd:YAG laser (wavelength = 356 nm) and the sample thickness was 4 μm.

Dielectric relaxation spectra of compound 6

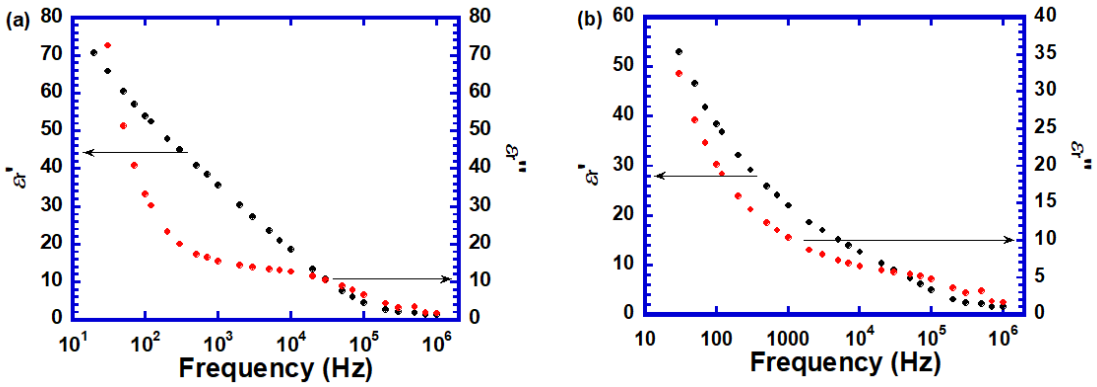

Figure S7 Dielectric relaxation spectra (a) in the non-polarized M* phase and (b) polarized M* phase of compound **6** at room temperature.

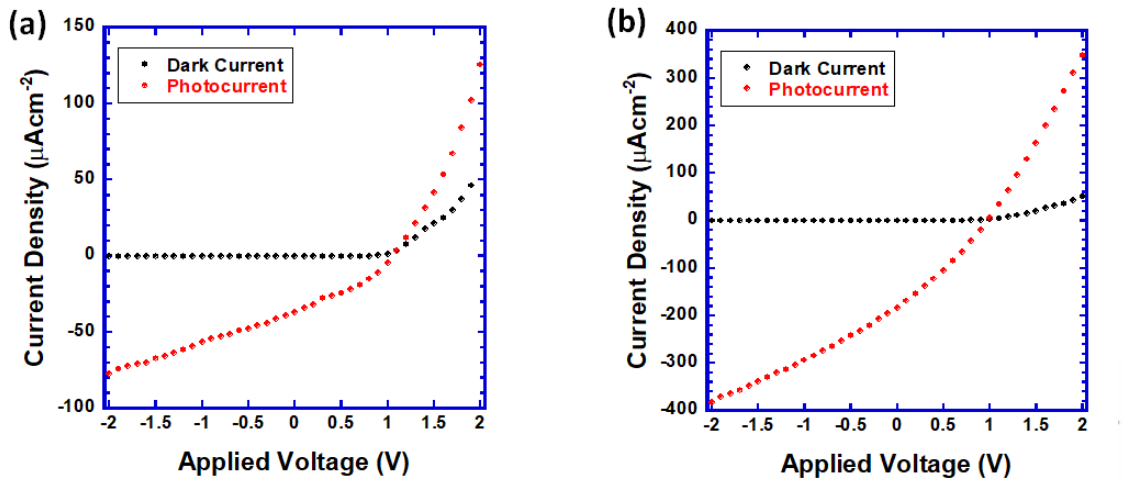

Figure S8 Current-voltage characteristics in the positively polarized M* phase of (a) pure (*S*,*S*)-**1** and (b) (*S*,*S*)-**1** doped with PCBM (8wt%) when AM1.5 (100 mW·cm^{-2}) was illuminated at room temperature. The sample thickness was 4 μm.

Table S2 Photovoltaic parameters of pure and PCBM-doped (8 wt%) compound (*S*,*S*)-**1** for AM1.5 illumination (100 mW·cm^{-2}).

	Open-circuit Voltage/ V	Short-circuit current density/ μAcm^{-2}	Fill factor	Power conversion efficiency/ %
Pure (*S*,*S*)-**1**	1.07	37.0	0.33	0.013
PCBM-doped (*S*,*S*)-**1**	0.98	183	0.29	0.05